

Cite this: *Mater. Adv.*, 2026,
7, 3747

Rice husk biochar-boosted BiOCl nanoplates: a sunlight-responsive route to wastewater detoxification and pathway insights for methylene blue degradation

Lovneet Kaur,[†] Palkaran Sethi[†] and Soumen Basu *

Heterojunction photocatalysts have attracted significant attention due to their ability to enhance pollutant degradation efficiency. In this study, bismuth oxychloride/rice husk biochar (BO/RB) heterojunction photocatalysts with different mass ratios (1:1, 1:3, and 3:1) were successfully synthesized via an *in situ* approach and comprehensively characterized using field emission scanning electron microscopy (FESEM), energy-dispersive X-ray spectroscopy (EDS), Fourier transform infrared spectroscopy (FTIR), X-ray photoelectron spectroscopy (XPS), X-ray diffraction (XRD), high-resolution transmission electron microscopy (HRTEM), ultraviolet-visible diffuse reflectance spectroscopy (UV-DRS), photoluminescence (PL) spectroscopy, and Brunauer–Emmett–Teller (BET) surface area analysis, confirming their structural integrity and high levels of porosity. The incorporation of RB onto BO broadened solar light absorption, enhanced charge carrier separation, and increased the surface area, resulting in improved photocatalytic degradation of methylene blue (MB). The degradation process was optimized by varying catalyst dosage, pollutant concentration, light source, pH, and contact time. Under optimized conditions, BR13 achieved 99% removal of 10 ppm MB within 100 min at pH ≥ 7 under sunlight, following pseudo-first-order kinetics with a rate constant of 0.01761 min^{-1} , exceeding that of commercial $\text{TiO}_2\text{-P25}$ (0.00922 min^{-1}). Reusability studies demonstrated good stability, retaining 92.3% degradation efficiency after five cycles. Radical scavenging experiments identified holes (h^+) and hydroxyl radicals ($\bullet\text{OH}$) as the dominant reactive species. Additionally, BR13 exhibited effective mineralization, achieving 62% COD and 55% TOC reduction for MB. Due to its high photocatalytic efficiency, stability, and simple synthesis, the BO/RB heterojunction shows strong potential for large-scale wastewater treatment and mitigation of persistent organic pollutants.

Received 11th November 2025,
Accepted 8th January 2026

DOI: 10.1039/d5ma01310k

rsc.li/materials-advances

1. Introduction

A planet seemingly blue from space, Earth is paradoxically gripped by a crisis where drinkable water is exceptionally scarce—less than 1% of all freshwater is readily accessible for human use.¹ Rapid population growth and industrial expansion compound this challenge, as industries continue to release toxic pollutants^{2–4} such as methylene blue (MB) into lakes and rivers, threatening both people and aquatic ecosystems. MB resists natural degradation, disrupts sunlight penetration, and is connected to severe health issues, including toxicity and cancer.^{5,6} These toxicological concerns necessitate the development of efficient and sustainable treatment strategies for the complete removal and mineralization of MB from wastewater.

A variety of methods exist for removing synthetic dyes from wastewater, including adsorption,⁷ photocatalysis,⁸ biological processes,⁹ and membrane-based physical separation;¹⁰ nevertheless, many fall short in completely breaking down these pollutants.^{11,12} Photocatalytic degradation has emerged as a highly effective approach that uses light-activated catalysts to decompose complex dye molecules into non-toxic substances like carbon dioxide and water. This process involves three main steps: the catalyst absorbs photons to create reactive electron-hole pairs, these reactive species initiate oxidation-reduction reactions, and the dyes are ultimately mineralized through direct or indirect photocatalytic pathways.^{13,14} Photocatalysis offers the advantage of mineralizing dyes without generating secondary waste, making it a sustainable approach for treating dye-contaminated water.^{15,16}

In recent years, rice husk biochar has emerged as a promising, economical, eco-friendly material for the removal of pollutants from water.¹⁷ Rice husk biochar, being rich in carbon,

Department of Chemistry and Biochemistry, Thapar Institute of Engineering & Technology, Patiala-147004, India. E-mail: soumen.basu@thapar.edu

[†] Both authors contributed equally.



silica, and functional groups, offers a high surface area, excellent pollutant adsorption capacity, and potential light-harvesting ability.^{18,19} A wide range of metal oxides, including zinc oxide (ZnO),^{20,21} titanium dioxide (TiO₂), bismuth oxychloride (BiOCl), iron oxide (Fe₂O₃), copper oxide (CuO), and tin oxide (SnO₂), and ferrite-based photocatalysts, including Fe₃O₄ and CoFe₂O₄ which offer the advantage of magnetic recovery, have been extensively studied for their photocatalytic abilities in degrading synthetic dyes, but their surface area and visible-light activity often require enhancement *via* composite formation.^{22–24} However, a common challenge among these materials is their wide band gap, which limits light absorption mainly to the UV region, reducing overall efficiency.²⁵ To overcome this, numerous approaches have been employed to narrow the band gap and improve photocatalytic efficiency, including metal or non-metal ion doping, coupling with conductive polymers, and forming composites with carbon-based materials like graphene, carbon nanotubes, or biochar. These modifications improve charge separation, increase visible light absorption, and boost degradation rates of dyes under sunlight or artificial light sources.^{26,27}

Eltaweil *et al.* synthesized a silver-loaded biochar nanocomposite (Ag@biochar), achieving 88.4% removal of methylene blue and retaining 70.65% efficiency after six reuse cycles.²⁸ Yu *et al.* synthesized ZnO/biochar nanocomposites *via* a simple ball-milling method, achieving 95.19% removal of methylene blue at a starting concentration of 160 mg L⁻¹ under visible light through combined adsorption and photocatalysis.²⁹ Sun *et al.* fabricated a g-C₃N₄/Ni_{0.1}Co_{0.9}Fe₂O₄/biochar hybrid photocatalyst, achieving 96.7% breakdown of methylene blue within 2 hours under visible light in the presence of H₂O₂.³⁰ Eswaran *et al.* reported the successful preparation of a zinc oxide-coated biochar nanocomposite, demonstrating its remarkable potential as a photocatalyst for the degradation of methylene blue under sunlight, achieving up to 92% efficiency.³¹ Sharma *et al.* developed a CeO₂/BiOCl/Ag₂WO₄ heterojunction photocatalyst that rapidly degraded methylene blue within 75 minutes.³² Adenuga *et al.* developed Ag/AgCl/BiOCl, showing 52% pollutant degradation under visible light.³³ Dong *et al.* synthesized BiOCl/reduced graphene oxide (BiOCl/RGO) composites, showing photocatalytic degradation of sulfanilamide (SN) with an 82.7% degradation rate.³⁴ He *et al.* demonstrated that Fe-doped BiOCl hierarchical microspheres significantly enhance visible-light-driven photocatalytic degradation of methylene blue, achieving a 93.5% removal efficiency.³⁵ Although these catalysts have shown encouraging outcomes, they typically exhibit relatively low degradation efficiencies for organic dyes and require prolonged light irradiation. Additionally, issues such as sluggish reaction kinetics, poor reusability, restricted operational pH ranges, and incomplete pollutant mineralization limit their effectiveness and practical applicability in environmental remediation.

The present study introduces a novel BiOCl/Rice Husk Biochar (BR) nanocomposite synthesized *via* a hydrothermal route, which has not been previously reported for photocatalytic applications. Unlike previously reported systems, this study uniquely couples carbon-rich rice husk biochar, a renewable

agricultural by-product, with semiconducting BiOCl, creating a synergistic hybrid material. The incorporation of biochar enhances surface area, pollutant adsorption, and charge transfer, while effectively narrowing the band gap of BiOCl and extending its response into the visible region. This synergistic interaction enhances charge carrier separation, suppresses electron-hole recombination, and significantly boosts photocatalytic activity. Remarkably, the BR nanocomposite exhibits its maximum degradation efficiency under natural sunlight, demonstrating its potential for real-world, solar-driven wastewater treatment. To the best of our knowledge, this is the first report of a BiOCl/rice husk biochar hybrid photocatalyst for methylene blue degradation under natural sunlight, highlighting its potential as a sustainable, cost-effective, and high-performance material for wastewater remediation. The composites were extensively characterized (XRD, XPS, FTIR, FESEM-EDS, HRTEM, UV-DRS, and PL), and key photocatalytic parameters, including catalyst dose, light source, solution pH, degradation kinetics, and scavenger studies, were systematically analyzed. Intermediates and final degradation products were identified by HRMS, and mineralization was confirmed by TOC and COD analyses. The optimized BR composites exhibited fast degradation rates, remarkable reusability, and superior solar-driven efficiency, successfully addressing prior constraints and offering a scalable, sustainable option for wastewater treatment.

2. Materials and methods

2.1. Materials

The chemicals and raw materials used are listed in the SI, S1.

2.2. Synthesis of BiOCl (BO)

A total of 242 mg of bismuth nitrate pentahydrate was dissolved in 100 mL of DI water with the addition of 1 mL of nitric acid to facilitate complete dissolution. The resulting solution was subjected to ultrasonication for 30 min, after which 37 mg of potassium chloride was added. The mixture was continuously stirred for 4 h and then centrifuged. The precipitate obtained was washed three times with distilled water and ethanol, then dried at 60 °C for 24 h to yield the final white powder.³⁶

2.3. Synthesis of rice husk biochar (RB)

The rice husk sample was thoroughly washed with distilled water and dried in an oven at 70 °C overnight to remove residual moisture. The dried material was then ground into a fine powder. 2 g of dried material was then sonicated in 50 mL DI water for 30 min and subjected to a hydrothermal reaction in a Teflon-lined autoclave at 200 °C for 24 hours, resulting in the formation of rice husk biochar. Then it was thoroughly washed with distilled water to remove impurities. The products were then dried in an oven. Then the dried samples were preserved in desiccators to avoid further absorption of moisture.



2.4. Synthesis of BiOCl/rice husk biochar composites

The composites were synthesized *via* an *in situ* method using different weight ratios of bismuth nitrate pentahydrate and porous biochar. For the representative 1:1 ratio, 485 mg of bismuth nitrate pentahydrate was dissolved in 200 mL of DI water, followed by the addition of 2 mL concentrated nitric acid to facilitate complete dissolution and suppress hydrolysis of Bi³⁺ ions. Then, 180 mg of RB was introduced into the solution, and the mixture was ultrasonicated for 30 min. Subsequently, 74 mg of KCl was added, and the reaction mixture was stirred continuously for 4 h to ensure appropriate interaction of all components. The same procedure was applied for other weight ratios (1:3 and 3:1) with appropriately adjusted amounts of reagents. The final suspension was centrifuged, and the collected precipitate was washed three times with distilled water and ethanol to eliminate any unreacted species and residual by-products. The purified material was dried in a hot air oven at 60 °C to obtain the powdered product. By altering the relative amounts of Bi(NO₃)₃·5H₂O, KCl, and biochar, hybrid composites with weight ratios of 1:1, 1:3, and 3:1 were successfully prepared and labelled as BR11, BR13, and BR31, respectively. The synthetic procedure for the BR hybrid is depicted schematically in Scheme 1.

3. Results and discussion

3.1. Characterization methods

Detailed descriptions of the characterization techniques employed in this study are provided in the supplementary material S2.

3.1.1. X-ray diffraction study. The crystalline structures of RB, BO, and their composites were examined using XRD

patterns (Fig. 1a). The diffraction peaks observed at $2\theta = 11.99^\circ$, 24.12° , 25.87° , 32.54° , 33.46° , 36.52° , 40.90° , 46.67° , 49.71° , 55.06° , and 58.63° correspond to the crystal planes (001), (002), (101), (110), (102), (003), (112), (200), (201), (004), (104), and (212), respectively. These diffraction peaks correspond well with the standard JCPDS card No. 06-0249, confirming the successful synthesis of BO nanoplates with a tetragonal crystal structure.³⁷ The strong preferential orientation along the (001) plane indicates the formation of stacked nanosheet-like structures, which is consistent with the layered nature of BO. In the case of RB, the XRD pattern confirmed the presence of amorphous silica, as evidenced by the broad hump around $2\theta \approx 21.48^\circ$ (002).³⁸ No additional impurity peaks were detected in the XRD patterns, confirming the successful fabrication of the composites. Furthermore, the negligible shift in peak positions suggests high phase purity of the binary heterojunction photocatalysts and confirms the coexistence of both phases in the composite.

3.1.2. FTIR measurements. FTIR spectroscopy was used to examine the surface functionalities and bonding characteristics of RB, BO, and their composites (Fig. 1b). The FTIR spectrum of BO typically exhibits a characteristic peak around 1128 cm^{-1} corresponding to the Bi–Cl stretching vibration, indicative of the bismuth oxychloride structure. Additionally, a broad band around 1609 cm^{-1} and one between 3200 and 3500 cm^{-1} correspond to the bending and stretching vibrations of hydroxyl groups and adsorbed water, indicating oxygen-containing surface functionalities vital for photocatalytic activity.^{39,40} The FTIR analysis of RB reveals specific functional groups characteristic of the material. Peaks in the range of 1619 – 1627 cm^{-1} likely indicate ketonic C=O groups, while a peak at 1568 cm^{-1} is associated with C–O⁺ stretching vibrations of oxonium groups, contributing to surface protonation. A distinct peak



Scheme 1 Schematic representation of the synthesis procedure of BR composites.



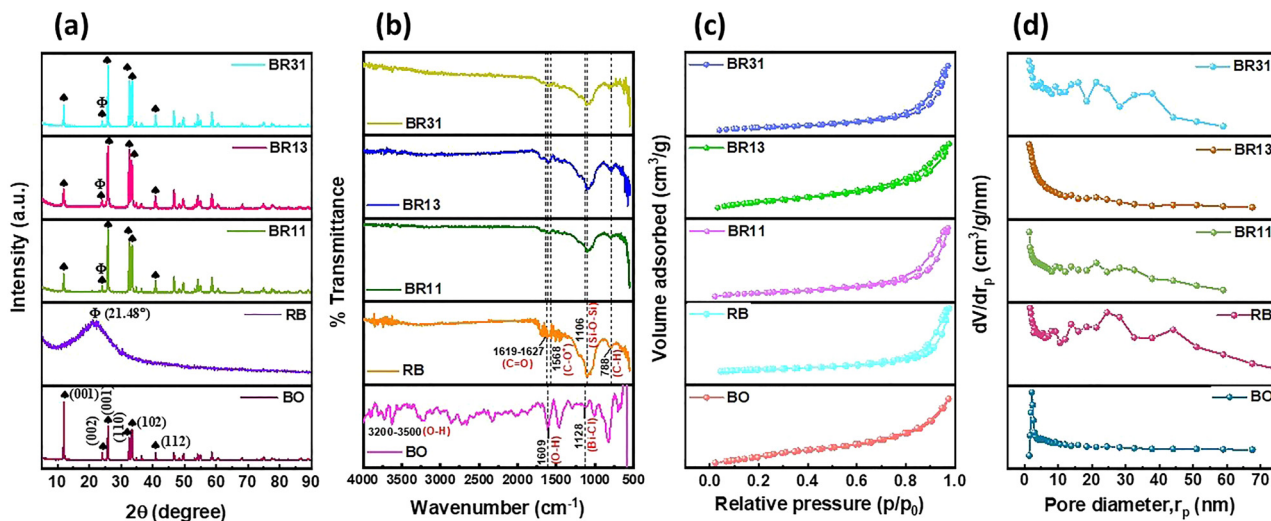


Fig. 1 (a) XRD pattern, (b) FTIR spectra, (c) N_2 adsorption–desorption isotherm curve and (d) BJH plot of BO, RB, BR11, BR13, and BR31.

at 1106 cm^{-1} , representing Si–O–Si stretching confirms the formation of biochar-derived silica during high-temperature calcination.⁴¹ The aromatic C–H symmetric stretching vibrations manifest near 1460 cm^{-1} , and out-of-plane aromatic C–H bending appears at 788 cm^{-1} (ref. 38). These spectral features correlate well with earlier XRD, confirming the composite's structural integrity and functionalization. Overall, the observed absorption bands, along with slight shifts in wavenumbers, confirm the coexistence of BiOCl and RB, and validate the successful synthesis of the nanocomposite.

3.1.3. BET surface area analysis. The specific surface area and porosity of the synthesized photocatalysts were evaluated using N_2 adsorption–desorption isotherms, as illustrated in Fig. 1c and summarized in Table 1. The adsorption–desorption profiles exhibited type IV isotherms for all samples, confirming the development of multilayer adsorption and capillary condensation within narrow pores. BJH analysis further revealed that the materials exhibit mesoporous characteristics, with pore diameters below 5 nm (Fig. 1d). The composites displayed larger pore volumes compared to the individual bulk counterparts. Notably, BO exhibited a relatively low surface area, whereas the incorporation of RB substantially enhanced the surface area in the composites, thereby promoting more effective adsorption.

3.1.4. UV-Vis DRS analysis. The light-harvesting ability and band gap energies of the photocatalysts were examined through

UV-Vis DRS measurements (Fig. 2a). The absorption edge of BO was observed in the wavelength range of 270–305 nm. The optical band gaps of the samples were determined using Tauc's relationship eqn (1):

$$(\alpha h\nu)^{1/2} = h\nu - E_g \quad (1)$$

where α denotes the absorption coefficient, h is Planck's constant, ν represents the frequency of incident light, and E_g corresponds to the optical band gap energy. The calculated band gap values for BO, RB, BR11, BR13, and BR31 were 3.46, 3.13, 2.24, 2.00, and 2.13, respectively (Fig. 2b). The positions of the valence band and conduction band of BO were further estimated using the following relationships:

$$E_{(\text{valence band})} = X - E_e + 0.5E_g \quad (2)$$

$$E_{(\text{conduction band})} = E_{\text{VB}} - E_g \quad (3)$$

Here, $E_{(\text{valence band})}$ and $E_{(\text{conduction band})}$ denote the valence band and conduction band energies, respectively, X is the absolute electronegativity of the semiconductor, and E_e is the reference energy of free electrons on the hydrogen scale, taken as 4.5 eV.⁴² Using these relationships, the $E_{(\text{valence band})}$ and $E_{(\text{conduction band})}$ values of BO were calculated to be 3.58 eV and 0.12 eV, respectively. RB exhibited broad absorption across the entire visible region due to its amorphous carbon structure with conjugated π -electron systems, which endows it with light-harvesting ability and electron conductivity. The reduced band gap of the BR13 composites facilitates improved absorption in the visible spectrum, enabling more efficient utilization of solar light.

3.1.5. XPS analysis. X-ray photoelectron spectroscopy (XPS) was performed to investigate the elemental composition, chemical states, and surface electronic environment of BR13. The survey spectra confirmed the presence of Bi, C, N, O, and Cl (Fig. 3a). The C 1s spectra displayed multiple chemical environments at 284.2 eV and 285.2 eV, attributed to graphitic sp^2 carbon and C–O bonding, respectively (Fig. 3b). The N 1s

Table 1 BET analysis results including specific area, mean pore diameter, and mean pore volume

Catalyst	Specific area ($\text{m}^2\text{ g}^{-1}$)	Mean pore diameter (nm)	Mean pore volume ($\text{cm}^3\text{ g}^{-1}$)
BO	2.60	6.9	0.00446
RB	39.6	18.2	0.1807
BR11	17.6	13.8	0.0605
BR13	30.1	7.5	0.0866
BR31	8.64	14.3	0.0310



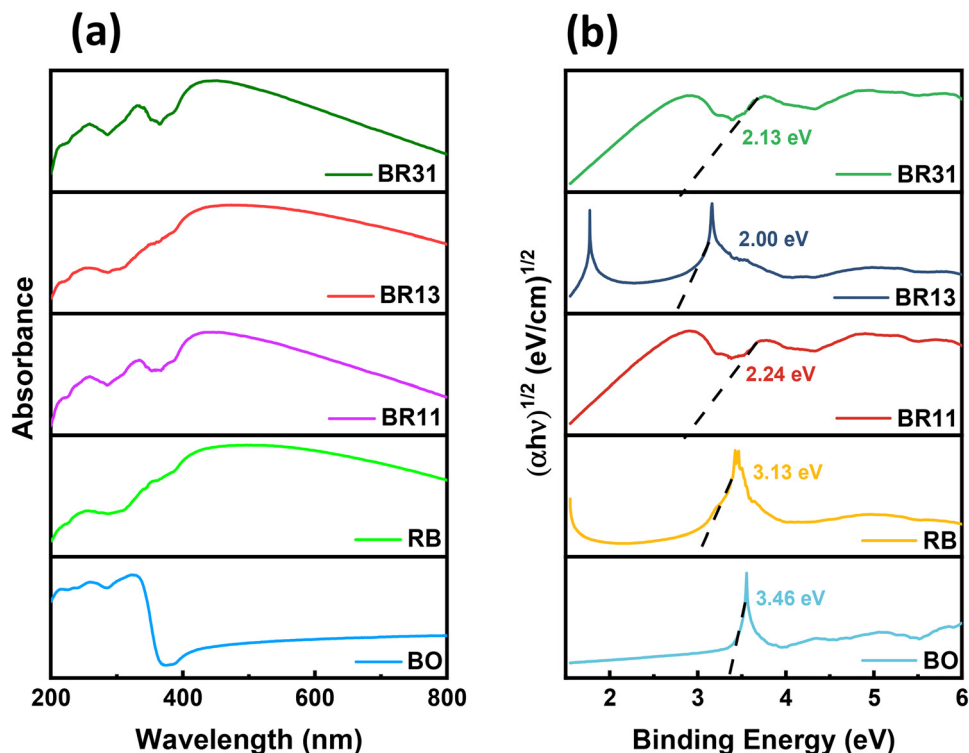


Fig. 2 (a) UV-vis DRS absorbance spectra, and (b) Tauc plot showing band gap energies of BO, RB, BR11, BR13, and BR31.

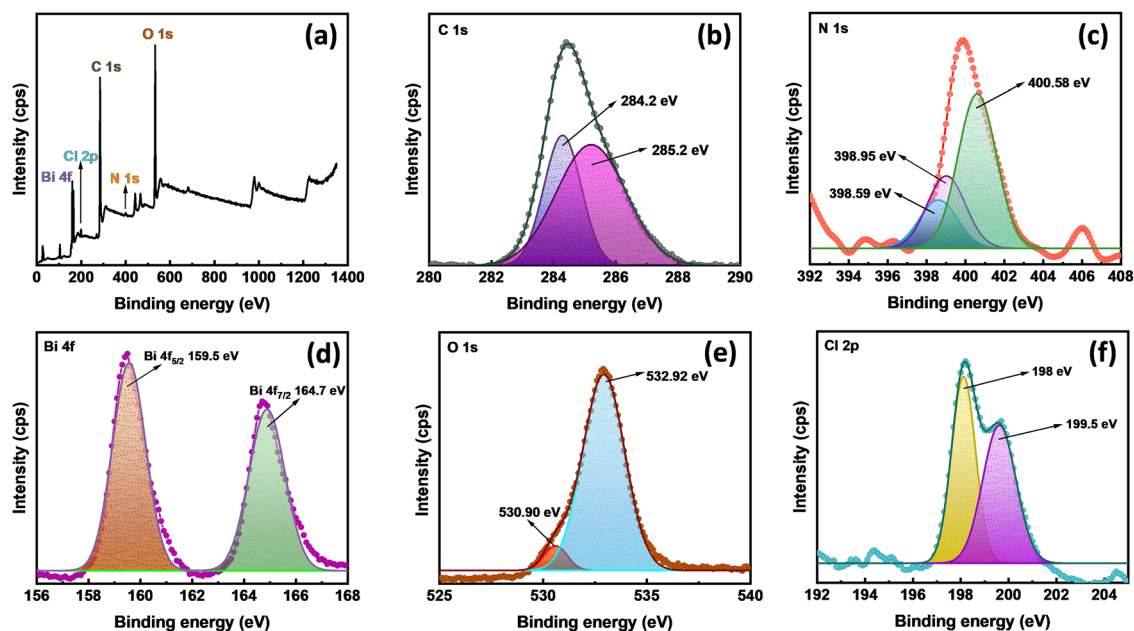


Fig. 3 XPS analysis of BR13 showing (a) a wide survey spectrum corresponding to (b) C 1s, (c) N 1s, (d) Bi 4f, (e) O 1s, and (f) Cl 2p regions.

spectrum also showed distinct features at 398.59 eV, 398.95 eV, and 400.58 eV (Fig. 3c). In the Bi 4f region, multiple peaks were observed at 159.5 eV and 164.7 eV corresponding to Bi 4f_{7/2} and Bi 4f_{5/2}, characteristic of Bi³⁺ in BO (Fig. 3d). In the O 1s region, the composite showed contributions from Bi–O bonds and

surface hydroxyls by peaks appearing at 530.90 eV (Bi–O bonds) and 532.92 eV (oxygen vacancies and surface hydroxyl groups) (Fig. 3e). The Cl 2p spectra confirmed the presence of chloride ions, with characteristic doublets at 198 eV and 199.5 eV which were assigned to Cl 2p_{3/2} and Cl 2p_{1/2} of Cl[−] ions bonded within



the BO lattice (Fig. 3f). Altogether, these XPS results verify the coexistence of Bi^{3+} , and carbon, nitrogen species, Bi–O bonding, hydroxyl groups, and chloride ions, confirming the successful formation and chemical composition of the composites.^{19,36,43} Such interactions not only stabilize the BO nanostructures on the RB surface but also promote efficient electron transfer pathways.

3.1.6. Morphological characterization. FESEM analysis was employed to gain insights into the morphological characteristics. Representative FESEM micrographs of BO, RB, and BR13

are shown in Fig. 4(a–c). The FESEM analysis of the BO component reveals that it forms rectangular nanoplates, showcasing a well-defined, angular morphology. In contrast, RB exhibited a fibrous morphology with a porous texture. In the nanocomposite BR13, RB was found to interact with BO sheets due to its fibrous framework, while the BO nanoplates were distinctly visible within the composite. These observations confirm the coexistence of BO and RB, indicating the successful fabrication of heterojunction structures. The elemental makeup of BR13 was further confirmed through energy-dispersive X-ray

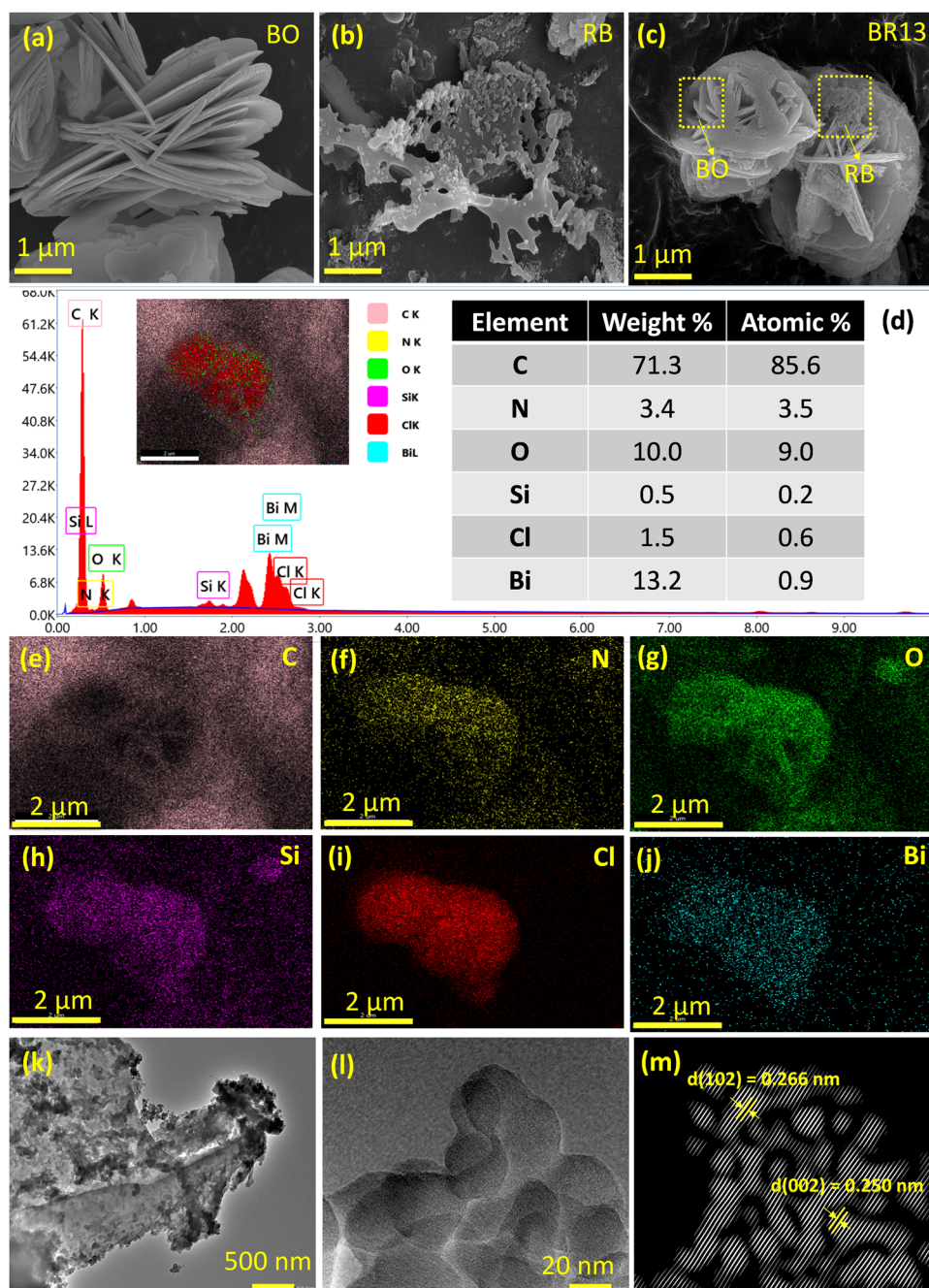


Fig. 4 FESEM images of (a) BO, (b) RB, (c) BR13, (d) EDS mapping, (e)–(j) colour mapping of all the elements present, (k) and (l) HRTEM images of BR13 at different magnifications and (m) calculated lattice fringes of BR13.



spectroscopy (EDS) analysis. EDS spectra confirmed the presence of C, N, Bi, O, Cl, and Si, while elemental coloured mapping demonstrated uniform spatial distribution of these elements, supporting the improved photocatalytic performance of the composite (Fig. 4(d–j)).

Furthermore, High-Resolution Transmission Electron Microscopy (HR-TEM) analysis revealed detailed structural features, confirming the formation of a porous, sheet-like morphology in Fig. 4(k and l). Fig. 4(m) displays aggregated nanoparticles, and high-resolution imaging revealed distinct lattice fringes corresponding to the (102) and (002) planes. The measured *d*-spacings were 0.266 nm for BO ($2\theta = 33.61^\circ$) and 0.250 nm for RB ($2\theta = 21.48^\circ$), confirming the crystalline nature of the respective components within the composite. The interplanar spacing observed from HRTEM lattice fringes is in good agreement with the corresponding planes identified in the XRD analysis. Overall, FESEM-EDS and HRTEM analyses validate the successful formation of the BR13 composite with uniform distribution, strong interfacial contact, and a porous heterojunction structure that is highly beneficial for photocatalytic applications. Particle size analysis was carried out using ImageJ software based on FESEM micrographs. The analysis was performed by measuring the diameters of randomly selected particles to ensure statistical reliability. The resulting particle size distribution histogram indicates a narrow size distribution, with an average particle size of approximately 34.04 nm, confirming the uniform morphology of the synthesized material. The nanoscale dimensions observed are in good agreement with the structural features evident from the HRTEM analysis (35.45 nm), confirming consistency between morphological and high-resolution structural characterization (Fig. S1).

3.1.7. Photoluminescence (PL) analysis. PL spectroscopy was employed to investigate the charge carrier recombination behavior in the synthesized samples.⁴⁴ Pristine BO exhibited a strong and sharp emission peak, signifying a high rate of recombination between photogenerated electron–hole pairs. Such high recombination severely limits its photocatalytic performance. In contrast, RB displayed a very weak PL signal due to its amorphous carbon nature, which acts as an electron reservoir and does not significantly contribute to radiative recombination. Notably, the BR composites demonstrated a markedly reduced PL intensity compared with pristine BO and RB, whereas BR13 showed the lowest PL intensity, signifying the effective suppression of charge carrier recombination at the heterojunction interface. The decrease in PL intensity can be ascribed to the efficient transfer of photoexcited electrons from BO to the conductive carbon matrix of RB, where they are stabilized and participate in subsequent redox reactions. This charge separation mechanism is further supported by the oxygenated functional groups present on RB, which act as anchoring sites and promote interfacial electron migration (Fig. 6a). The suppressed PL emission intensity of the composites directly correlates with their enhanced photocatalytic activity, confirming that the synergistic interaction between BO nanosheets and RB facilitates charge separation, prolongs

carrier lifetimes, and thereby improves the efficiency of pollutant degradation under light irradiation.

3.2. Photocatalytic activity

The photocatalytic performance of BR13 was assessed through the degradation of MB dye. For each experiment, a 10 mL MB solution (10 ppm) was used with a catalyst dosage of 0.2 g L⁻¹. To attain adsorption–desorption equilibrium, the mixture was stirred in the dark for 120 minutes before exposure to light. Subsequently, the photocatalytic reactions were carried out under natural sunlight in August 2025 on clear, sunny days within a fixed time window for a duration of 100 min. To further study the effect of light irradiation, an artificial illumination test was performed using a 45 W Philips lamp (radiant flux ≈ 100 W m⁻²), positioned 10 cm above the reaction mixture. A control experiment was also conducted under dark conditions for 120 min and was performed while maintaining identical experimental parameters.

Each experiment was conducted in triplicate, and the resulting data are represented with error bars showing approximately $\pm 5\%$ variation. The degradation of MB was monitored by recording its absorbance at 659 nm using a UV-visible spectrophotometer as shown in Fig. S2, the characteristic absorption peak of MB gradually decreased with increasing irradiation time, indicating effective degradation of the dye molecules rather than mere adsorption, and the degradation efficiency (%) was computed using the following eqn (4).

$$\text{Degradation efficiency} = \frac{A_0 - A_f}{A_0} \times 100 \quad (4)$$

where A_0 represents the initial absorbance of the MB solution before irradiation, and A_f denotes the final concentration after the degradation process.

To evaluate the performance of the synthesized nanocomposite, a comparative study was performed against TiO₂ (P25, a commercial photocatalyst), BO, RB, BR11, BR13, and BR31 (Fig. 5(a) and (b)). In contrast, only a very small extent of degradation was observed in the absence of the photocatalyst, confirming that the process was predominantly photocatalytic in nature (Fig. 5(c) and (d)). The apparent rate constant (*k*) for the photocatalytic degradation process was determined using the following eqn (5).

$$\ln \frac{A}{A_0} = -kt \quad (5)$$

Here, A_0 represents the initial concentration of dye, *A* is the concentration at a given time *t*, and *k* denotes the apparent rate constant of the reaction. Based on the plots in Fig. 6(b), the degradation process was observed to follow pseudo-first-order kinetics. The BR13 composite exhibited the highest efficiency, with a rate constant of 0.01761 min⁻¹, which is considerably greater than that of bare BO (0.00425 min⁻¹), RB (0.01032 min⁻¹), BR11 (0.00907 min⁻¹), and BR31 (0.00681 min⁻¹). To further understand the cooperative effect among the composite



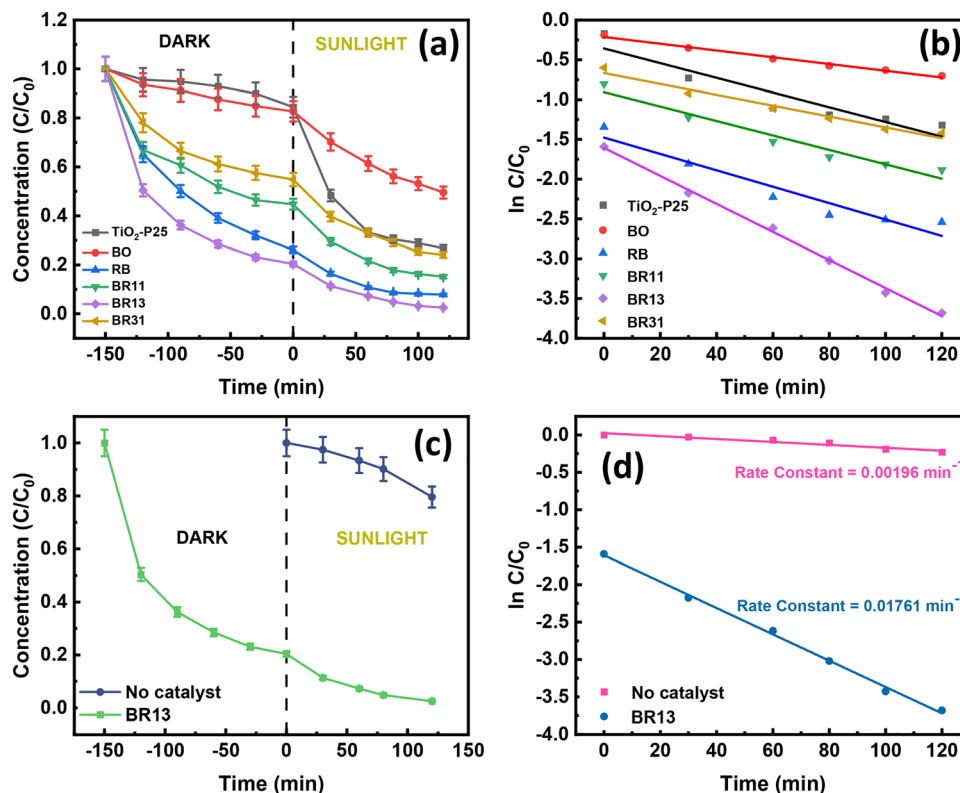


Fig. 5 (a) and (b) Kinetic examination of the different fabricated catalysts for the remediation of MB. (c) and (d) Kinetic analysis of the degradation of MB with and without a catalyst.

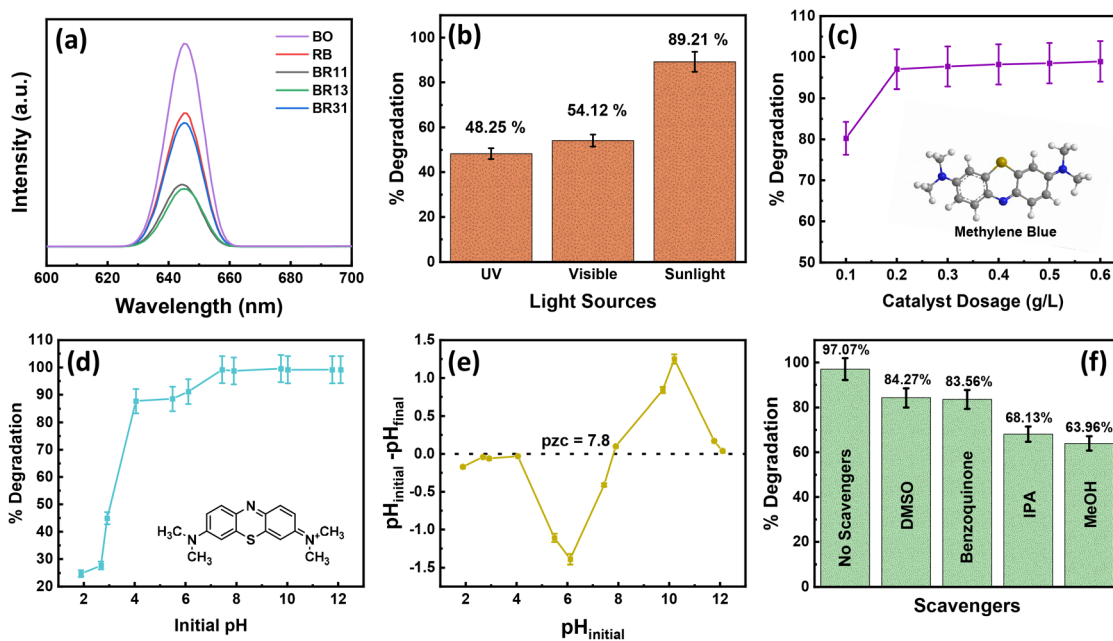


Fig. 6 (a) Photoluminescence (PL) spectra, (b) changes in degradation of MB under different light intensities, (c) effect of catalyst loading towards MB, (d) effect of pH on MB removal, (e) pzc studies, and (f) scavenger studies.

components, the synergy factor (R) was calculated using eqn (6).

$$R = \frac{K_{BO+RB}}{K_{BO} + K_{RB}} \quad (6)$$

In this context, K_{BO+RB} , K_{BO} , and K_{RB} represent the photo-degradation rate constants of the BR composites, pristine BO, and pristine RB, respectively. The calculated synergy factors for



Table 2 MB degradation synergy factors (R) and rate constants (k)

Material	Rate constant (min^{-1})	Synergy factor (R)
TiO ₂ -P25	0.00922	—
BO	0.00425	—
RB	0.01032	—
BR11	0.00907	0.6225
BR13	0.01761	1.2086
BR31	0.00681	0.4674

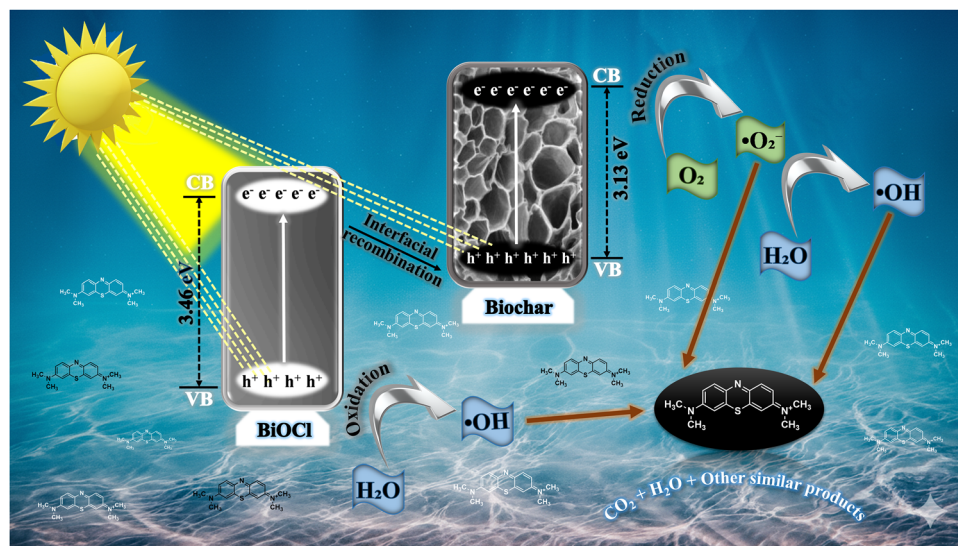
BR11, BR13, and BR31 were 0.6225, 1.2086, and 0.4674, which revealed that BR13 exhibited the highest value, indicating the strongest interfacial interaction between its components. This enhanced synergy explains its superior photocatalytic efficiency and the highest observed rate constant among all the prepared nanocomposites (Table 2).

3.2.1. Effect of light sources. Comparative photocatalytic tests were performed under UV, visible, and natural sunlight to evaluate pollutant degradation. As illustrated in Fig. 6b, the BR13 (0.1 g L^{-1}) heterojunction photocatalyst achieved 48% degradation under UV light and 54% under visible light, and a maximum of 89% under sunlight. These findings demonstrate that sunlight provides the most effective conditions for pollutant breakdown using this photocatalyst, confirming its superior performance.

3.2.2. Impact of the catalyst dose. The influence of catalyst dosage on photocatalytic performance was investigated by varying the concentration from 0.1 to 0.6 g L^{-1} under sunlight. The degradation efficiency increased steadily with catalyst loading up to 0.2 g L^{-1} , beyond which it reached a plateau (Fig. 6c). This saturation effect was attributed to the reduced transparency of the dye solution, which hindered light penetration and partially blocked the active sites of the photocatalyst. Additionally, the deactivation of active sites may also limit photocatalytic activity at elevated concentrations. Thus, 0.2 g L^{-1} was determined as the most effective catalyst dosage for subsequent studies.

3.2.3. Impact of pH. pH strongly governs photocatalytic degradation by influencing catalyst surface charge and dye-catalyst interactions. The point of zero charge (PZC) of the photocatalyst was found to be 7.8 (Fig. 6e). At pH values below this point, the catalyst surface carries a positive charge, whereas at pH values above 7, it becomes negatively charged. Since methylene blue (MB) is a cationic dye, electrostatic repulsion occurs under acidic conditions ($\text{pH} < 7$), resulting in reduced adsorption and degradation efficiency. In contrast, under neutral to alkaline conditions ($\text{pH} \geq 7$), the negatively charged catalyst surface strongly attracts the positively charged MB molecules, enhancing adsorption and accelerating photocatalytic degradation. As shown in Fig. 6d, degradation efficiency increased significantly under alkaline conditions, achieving up to 99.71% removal efficiency above pH 7, confirming that the photocatalyst exhibits optimal performance in basic media for MB wastewater treatment. Consequently, maximum removal efficiency is achieved in basic media, highlighting the catalyst's suitability for MB wastewater treatment.

3.2.4. Effect of scavengers on photocatalytic activity. The photocatalytic mechanism was further investigated by performing scavenger experiments to identify the primary reactive species involved in the degradation process. Different radical scavengers were introduced into the reaction system: isopropanol (IPA) for hydroxyl radicals ($\cdot\text{OH}$), benzoquinone (BQ) for superoxide radicals ($\cdot\text{O}_2^-$), methanol (MeOH) for holes (h^+), and dimethyl sulfoxide (DMSO) for electrons (e^-).⁷ The interaction of $\text{O}_2\cdot^-$ with BQ results in the formation of hydroquinone, confirming the role of superoxide radicals. The strong inhibition observed in the presence of DMSO indicates the pivotal involvement of hydroxyl radicals, as DMSO readily undergoes electron transfer *via* its unpaired oxygen electrons and forms hydrogen bonds with $\cdot\text{OH}$ radicals. As depicted in Fig. 6f, the addition of methanol and IPA significantly reduced the degradation efficiency, demonstrating that photogenerated

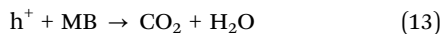
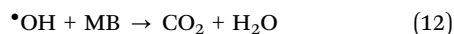
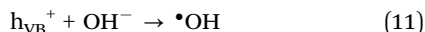
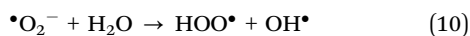


Scheme 2 Proposed mechanism illustrating the photocatalytic degradation pathway of MB over the BR13 composite under light irradiation.



holes and hydroxyl radicals are the primary reactive species responsible for the photocatalytic degradation, while the contributions of other species are comparatively minor.

3.2.5. Proposed photocatalytic mechanism. Upon sunlight irradiation, e^- in the CB of BO can migrate back to its VB, and similarly, e^- from the CB of RB can also move to its own VB. This process leads to an interfacial recombination where e^- in the VB of BO recombine with h^+ in the CB of RB. Such recombination at the interface helps reduce charge carrier recombination elsewhere, enhancing overall photocatalytic efficiency (Scheme 2). When holes and hydroxyl radicals are the primary reactive species in degradation, the process involves these charge carriers oxidizing pollutants through the following key reactions (7)–(13):



This mechanism highlights the crucial role of interfacial charge transfer and recombination dynamics in generating active oxidative species, leading to efficient photocatalytic degradation.

3.3.6. Reusability study. The long-term stability and recyclability of a photocatalyst are essential parameters for its practical application in wastewater treatment. To assess the reusability of the BR13 composite, cyclic photocatalytic degradation experiments were conducted using MB under natural sunlight. After each cycle, the catalyst was separated from the reaction mixture by centrifugation, thoroughly washed with distilled water and ethanol to remove any residual dye or intermediate products, and then dried at 60 °C before reuse. As shown in Fig. 7(a), the degradation efficiency remained close to 92% even after five consecutive cycles, demonstrating excellent reusability. The observed decline in activity, from 99% to 92%, can be ascribed to minor catalyst loss during recovery and the surface accumulation of undegraded intermediates, which may partially block the pores and active sites. Moreover, the structural stability of the reused BR13 photocatalyst was validated by X-ray diffraction analysis after five cycles (Fig. 7e), where the diffraction peaks retained their positions and intensities without the emergence of any new peaks, confirming the preservation of its crystalline framework. Furthermore, BET surface analysis (Fig. 7c) revealed a pore volume of 0.1059 $\text{cm}^3 \text{g}^{-1}$, a specific area of 25.992 $\text{m}^2 \text{g}^{-1}$, and a mean pore diameter of 16.296 nm for the recycled photocatalyst. Although a slight reduction in surface area was observed, it remained sufficient for effective photocatalytic activity. FESEM micrographs (Fig. 7d), EDS, and colour mapping further confirmed that the morphology and the distribution of elements of the composite remained unchanged after repeated use. These findings highlight that the BR13 photocatalyst exhibits remarkable durability, structural integrity, and strong reusability,

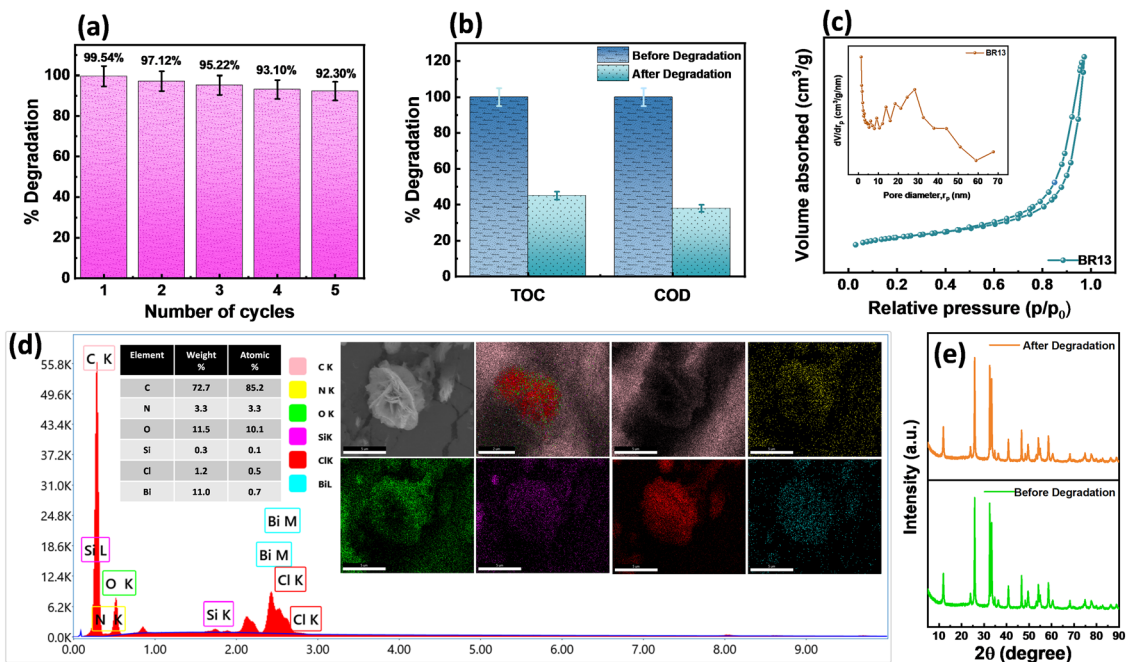


Fig. 7 (a) Cyclic degradation performance of BR13 demonstrating excellent recyclability, (b) comparative TOC and COD analyses, and (c) BET surface area analysis with the inset showing the Barrett–Joyner–Halenda pore size distribution curve of the BR13 photocatalyst after degradation activity, (d) FESEM images and EDS elemental colour mapping of the BR13 photocatalyst after degradation studies, and (e) XRD analysis after five cycles.



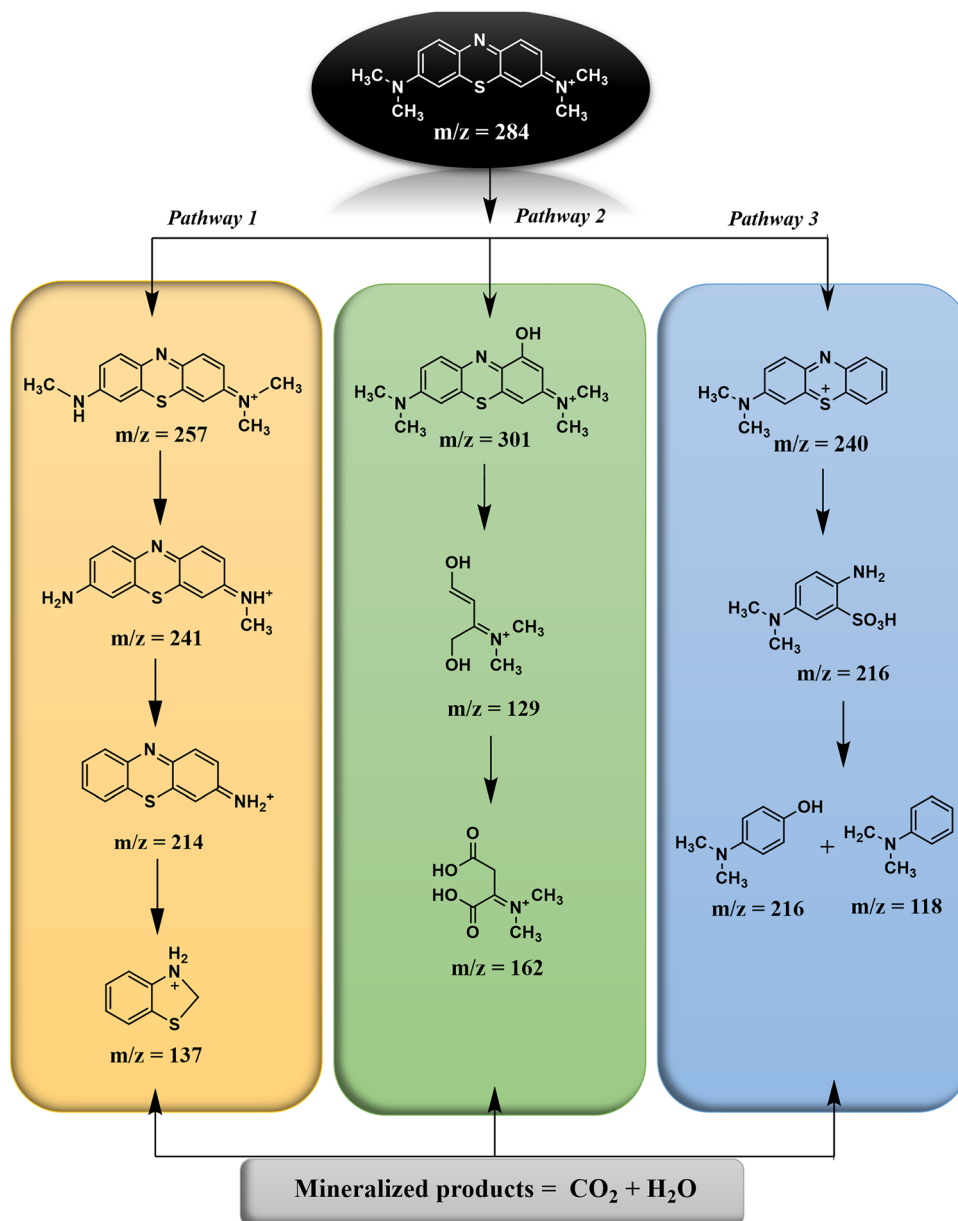
establishing it as a suitable composite for long-term photocatalytic environmental remediation application.

3.2.7. Mineralization studies. To evaluate the extent of complete degradation of methylene blue (MB) and confirm its conversion into non-toxic end products, total organic carbon (TOC) and chemical oxygen demand (COD) analyses were performed after photocatalytic treatment. After 100 minutes of sunlight irradiation, TOC and COD removal efficiencies for MB were recorded as 55% and 62%, respectively. As illustrated in Fig. 7(b), the solution underwent progressive mineralization, although the persistence of intermediate species with low mineralization potential was evident. The presence of these partially oxidized organic compounds before the complete conversion of MB into CO_2 , H_2O and other byproducts accounts

for the lower TOC and COD reduction compared to the overall degradation rate.

3.2.8. Probable degradation pathway of MB. High-resolution mass spectrometry (HRMS) analysis was performed to identify the intermediate and final degradation products formed during the photocatalytic oxidation of methylene blue (MB). The corresponding HRMS spectra are presented in Fig. S3. Multiple intermediate peaks with varying m/z values confirmed the stepwise decomposition of MB molecules. Based on the detected fragments and their molecular ion peaks, three predominant degradation pathways were proposed, as illustrated in Scheme 3.

Pathway I: the degradation of methylene blue ($m/z = 284$) begins with stepwise demethylation of the molecule. Initially, a



Scheme 3 Proposed degradation pathway of MB.



Table 3 Comparison of different photocatalysts used for the degradation of MB

Photocatalyst	Pollutant decomposed	Catalyst dose (g L ⁻¹)	Illuminating source	Time (min)	% Degradation	Ref.
rGO/NiO _x /Ag	Methylene blue	0.5	Sunlight	90	91	48
TiO ₂ /CNTs	Methylene blue	0.2	Visible	180	85	49
RGO/CDs (RC)	Methylene blue	0.1	Visible	135	87	50
NiO/g-G ₃ N ₄	Methylene blue	0.1	Sunlight	180	91	51
FeWO ₄ @N-TiO ₂	Methylene blue	0.2	Visible light	120	77	52
CuS/ZnS	Methylene blue	0.6	Visible light	85	90	53
Bi ₂ CrO ₆ /CuO	Methylene blue	—	Visible light	120	90.06	54
α-Fe ₂ O ₃ /ZnO	Methylene blue	1.0	UV light	105	85	55
BiOCl/rice husk biochar (1:3)	Methylene blue	0.2	Sunlight	100	99	Present work

methyl group (-CH₃) is removed, yielding a product at $m/z = 257$ and 241, corresponding to the gradual removal of methyl groups from the nitrogen atoms. Further demethylation or reduction transforms the molecule into amine-containing intermediates at $m/z = 214$, where additional hydrogen or methyl substitutions generate amino-functionalized species. The pathway then progresses through cleavage of the central aromatic ring or heterocyclic structure, producing a smaller intermediate at $m/z = 138$, identified as protonated phenyl thiophene. Finally, complete mineralization of this intermediate occurs, resulting in the formation of inorganic end products such as CO₂ and H₂O.⁴⁵

Pathway II: the first step involves hydroxylation, introducing an -OH group into the structure, which increases its mass to $m/z = 301$. Subsequent oxidative cleavage of the aromatic rings generates smaller intermediates. One of these is a molecule with $m/z = 129$, which is a partially degraded and functionalized fragment of the original structure, likely containing hydroxyl and amino functionalities. Further oxidation leads to an intermediate at $m/z = 162$, containing carboxyl and hydroxyl groups. Finally, complete mineralization occurs, breaking the molecule down into CO₂ and H₂O, representing the total degradation of methylene blue into inorganic end products.⁴⁶

Pathway III: pathway 3 of the degradation process begins with the cleavage of the -N(CH₃)₂ group from the parent molecule, resulting in the formation of a product m/z of 240. Subsequently, oxidation of the sulfhydryl (C-S or C=S) groups occurs, which transforms into a fragment ($m/z = 216$). Further degradation takes place through desulfurization, oxidation, and deamination, producing additional fragments at $m/z = 137$ and $m/z = 118$. Overall, Pathway 3 involves sequential demethylation, ring cleavage, oxidation of sulfur-containing groups, and stepwise removal of functional groups, ultimately yielding a series of smaller, oxidized products detectable by their characteristic m/z values.⁴⁷

Comparison from the literature. To further evaluate the performance of the synthesized photocatalyst, a comparative analysis was conducted with previously reported photocatalysts. Table 3 summarizes the degradation efficiencies, and operational conditions of various photocatalytic systems reported in the literature, highlighting the superior activity and sunlight-driven performance of the present BR13 nanocomposite toward MB degradation.

4. Conclusion

In this work, a novel BiOCl/rice husk biochar (BR13) hetero-junction photocatalyst was successfully developed through an *in-situ* synthesis approach aimed at the efficient degradation of methylene blue (MB) dye from aqueous media. Extensive physico-chemical characterization, including XRD, FTIR, BET, FESEM-EDS, HRTEM, XPS, UV-DRS, and PL analyses, confirmed the uniform integration of biochar within the BiOCl framework, resulting in a stable composite with superior crystallinity, enhanced light-harvesting capability, and significantly increased specific surface area. Under solar irradiation, the optimized BR13 composite achieved nearly complete degradation (~99%) of a 10 ppm MB solution within 100 minutes, following pseudo-first-order kinetics with a rate constant of 0.01761 min⁻¹. This performance was 1.7 and 4.1 times higher than that of pristine RB and BO, respectively, and almost twice that of commercial TiO₂-P25, clearly demonstrating the synergistic enhancement and high photocatalytic activity. Systematic optimization of operational parameters, including catalyst dosage, pH, illumination conditions, and scavenger tests, revealed that photogenerated holes and hydroxyl radicals play dominant roles in the degradation mechanism. Furthermore, BR13 exhibited outstanding recyclability and structural durability, maintaining over 92% of its initial degradation efficiency after five successive cycles, as confirmed by post-reaction XRD analyses. Mineralization studies showed substantial TOC and COD reductions of 55% and 62%, respectively, indicating effective conversion of MB into environmentally benign products. HRMS analysis provided additional mechanistic insights by identifying intermediate species and outlining the stepwise degradation pathway. Overall, this study establishes BR13 as a robust, solar-active photocatalyst with scalable synthesis, strong structural integrity, and remarkable reusability, making it a highly promising candidate for practical wastewater remediation and broader applications in sustainable environmental purification technologies. Despite these advantages, the photocatalytic performance may be influenced by fluctuations in natural sunlight intensity, and complete mineralization is not achieved, indicating scope for further optimization toward real wastewater applications.

Author contributions

Loveneet Kaur: designed and performed the experiments, analysed data and co-wrote the paper. Palkaran Sethi: supervised



the research, designed experiments and co-wrote the paper. Soumen Basu: supervised the research and co-wrote the paper.

Conflicts of interest

The authors declare that there are no conflicts of interest, financial or personal, that could have influenced the research presented in this paper.

Data availability

All data supporting the findings of this study are available within the article and detailed list of materials used and characterisation techniques are listed in its supplementary information (SI). It also includes particle size distribution curve, UV visible spectra of methylene blue during different time intervals, and HRMS spectra for degradation pathway. See DOI: <https://doi.org/10.1039/d5ma01310k>.

Additional raw data, including characterization spectra (FESEM, EDS, FTIR, XPS, XRD, HRTEM, UV-DRS, PL, and BET) and photocatalytic degradation datasets, are available from the corresponding author upon reasonable request.

Acknowledgements

We sincerely acknowledge DCBC and DPMS, TIET, for providing the necessary infrastructure for the characterization studies. The Department of Chemical Engineering is gratefully recognized for making their UV-visible spectrophotometer available. Special thanks are extended to SAIF and CIL, Punjab University for the HR-TEM and XPS analysis and the Institute of Nano Science and Technology, Mohali, for providing FESEM-EDS facilities.

References

- J. N. Maduelosi and M. U. Ezuluofor, *Br. J. Multidiscip. Adv. Stud.*, 2023, **4**, 1–8.
- A. Tariq and A. Mushtaq, *Int. J. Chem. Biochem. Sci.*, 2023, **23**, 121–143.
- O. Cardoso, J.-M. Porcher and W. Sanchez, *Chemosphere*, 2014, **115**, 20–30.
- S. Thakur, A. Chandra, V. Kumar and S. Bharti, in *Bio-technology for Environmental Sustainability*, ed. P. Verma, Springer Nature Singapore, Singapore, 2025, pp. 55–100.
- S. Khan, T. Noor, N. Iqbal and L. Yaqoob, *ACS Omega*, 2024, **9**, 21751–21767.
- R. B. Chavan, *Health and Environmental Hazards of Synthetic Dyes*, 2013.
- P. Sethi, S. Basu and S. Barman, *New J. Chem.*, 2025, **49**, 8454–8471.
- H. Bansal, P. Sethi and S. Basu, *Mater. Adv.*, 2025, **6**(20), 7585–7598.
- P. V. Nidheesh, C. Couras, A. V. Karim and H. Nadais, *Chem. Eng. Commun.*, 2022, **209**, 390–432.
- S. K. Ramachandran and P. Sathishkumar, *Curr. Opin. Environ. Sci. Health*, 2023, **36**, 100513.
- K. Masula, P. Sreedhar, P. Vijay Kumar, Y. Bhongiri, S. Pola and M. Basude, *Mater. Sci. Semicond. Process.*, 2023, **160**, 107432.
- K. Kaur, R. Gade, R. Mitty, V. S. (Narayanabhatla) Puli, S. Pola and N. B. Simhachalam, *Surf. Interfaces*, 2025, **72**, 107254.
- B. Garg, P. Hait and S. Basu, *J. Environ. Manage.*, 2024, **370**, 122403.
- C. Maggu, S. Singla and S. Basu, *J. Environ. Manage.*, 2024, **349**, 119424.
- M. Subburu, R. Gade, V. Guguloth, P. Chetti, K. R. Ravulapelly and S. Pola, *J. Photochem. Photobiol., A*, 2021, **406**, 112996.
- R. Vallavoju, R. Kore, R. P. M. Subburu, M. Basude, P. Chetti and S. Pola, *J. Photochem. Photobiol., A*, 2023, **442**, 114775.
- M. Kordi, N. Farrokhi, M. I. Pech-Canul and A. Ahmadikhah, *Rice Sci.*, 2024, **31**, 14–32.
- Q. Liang, D. Pan and X. Zhang, *Chem. Eng. J.*, 2023, **453**, 139441.
- R. Nandi, M. K. Jha, S. K. Guchhait, D. Sutradhar and S. Yadav, *ACS Omega*, 2023, **8**, 4802–4812.
- P. Agale, V. Salve, S. Mardikar, S. Patange and P. More, *Appl. Surf. Sci.*, 2024, **672**, 160795.
- P. More, V. Inamdar, S. Suresh, S. Dindorkar, S. Peddakolmi, K. Jain, N. Khona, S. Khatoon and S. Patange, *J. Mater. Sci.: Mater. Electron.*, 2021, **32**, 20725–20741.
- K. Jangam, K. Patil, S. Balgude, S. Patange and P. More, *RSC Adv.*, 2020, **10**, 42766–42776.
- V. C. Pujari, P. D. Mhase, S. D. Balgude, S. S. Jadhav, S. J. Gilani, P. S. More, S. E. Shirsath, S. F. Shaikh and S. M. Patange, *Ceram. Int.*, 2025, **51**, 39866–39885.
- K. Jangam, S. Balgude, H. Pawar, S. Patange and P. More, *Surf. Interfaces*, 2022, **33**, 102189.
- E. Asgari, A. Esrafil, A. J. Jafari, R. R. Kalantary and M. Farzadkia, *Desalin. Water Treat.*, 2019, **161**, 228–242.
- A. Al Miad, S. P. Saikat, M. K. Alam, M. S. Hossain, N. M. Bahadur and S. Ahmed, *Nanoscale Adv.*, 2024, **6**(19), 4781–4803.
- P. Sethi, S. Barman and S. Basu, *ACS Sustainable Resour. Manage.*, 2026, **3**(1), 244–259.
- A. S. Eltaweil, A. M. Abdelfatah, M. Hosny and M. Fawzy, *ACS Omega*, 2022, **7**, 8046–8059.
- F. Yu, F. Tian, H. Zou, Z. Ye, C. Peng, J. Huang, Y. Zheng, Y. Zhang, Y. Yang, X. Wei and B. Gao, *J. Hazard. Mater.*, 2021, **415**, 125511.
- J. Sun, X. Lin, J. Xie, Y. Zhang, Q. Wang and Z. Ying, *Colloids Surf., A*, 2020, **606**, 125556.
- P. Eswaran, P. D. Madasamy, K. Pillay and H. Brink, *Biomass Convers. Biorefin.*, 2025, **15**, 12347–12367.
- K. Sharma, S. Sonu, A. Sudhaik, T. Ahamad, S. Kaya, S. Thakur, Q. Van Le, V.-H. Nguyen, A. Singh, L. H. Nguyen, P. Singh and P. Raizada, *J. Water Process Eng.*, 2024, **66**, 105918.
- D. O. Adenuga, S. M. Tichapondwa and E. M. N. Chirwa, *J. Photochem. Photobiol., A*, 2020, **401**, 112747.



- 34 S. Dong, Y. Pi, Q. Li, L. Hu, Y. Li, X. Han, J. Wang and J. Sun, *J. Alloys Compd.*, 2016, **663**, 1–9.
- 35 L. He, X. Wang and D. Hong, *Langmuir*, 2025, **41**, 21471–21482.
- 36 P. Hait, R. Mehta and S. Basu, *J. Clean Prod.*, 2023, **424**, 138851.
- 37 M. Guan, C. Xiao, J. Zhang, S. Fan, R. An, Q. Cheng, J. Xie, M. Zhou, B. Ye and Y. Xie, *J. Am. Chem. Soc.*, 2013, **135**, 10411–10417.
- 38 S. Aziz, B. Uzair, M. I. Ali, S. Anbreen, F. Umber, M. Khalid, A. A. A. Aljabali, Y. Mishra, V. Mishra, Á. Serrano-Aroca, G. A. Naikoo, M. El-Tanani, S. Haque, A. G. Almutary and M. M. Tambuwala, *Environ. Res.*, 2023, **238**, 116909.
- 39 W. Tang, Y. Zhang, H. Guo and Y. Liu, *RSC Adv.*, 2019, **9**, 14060–14071.
- 40 A. Kundu, S. Sharma and S. Basu, *J. Phys. Chem. Solids*, 2021, **154**, 110064.
- 41 P. T. Le, D. N. Le, T. H. Nguyen, H. T. Bui, L. A. Pham, L. L. Nguyen, Q. S. Nguyen, T. P. Nguyen, T. H. Dang, T. T. Duong, M. Herrmann, S. Ouillon, T. P. Q. Le, D. L. Vo, H. Mai and T. M. T. Dinh, *Water*, 2021, **13**(23), 3326.
- 42 D. Monga and S. Basu, *RSC Adv.*, 2021, **11**, 22585–22597.
- 43 K. Jasuja and R. K. Das, *Mater. Adv.*, 2025, **6**, 3957–3968.
- 44 A. A. B. Baloch, F. H. Alharbi, G. Grancini, M. I. Hossain, Md. K. Nazeeruddin and N. Tabet, *J. Phys. Chem. C*, 2018, **122**, 26805–26815.
- 45 L. O. de, B. Benetoli, B. M. Cadorin, V. Z. Baldissarelli, R. Geremias, I. G. de Souza and N. A. Debacher, *J. Hazard. Mater.*, 2012, **237–238**, 55–62.
- 46 H. W. P. Carvalho, A. P. L. Batista, P. Hammer and T. C. Ramalho, *J. Hazard. Mater.*, 2010, **184**, 273–280.
- 47 Y. Sun, S. Tu, Y. Li, X. Sui, S. Geng, H. Wang, X. Duan and L. Chang, *Colloids Surf., A*, 2024, **690**, 133861.
- 48 D. Singh, K. M. Batoor, S. Hussain, A. Kumar, Q. H. Aziz, F. S. Sheri, H. Tariq and P. Singh, *RSC Adv.*, 2024, **14**, 2429–2438.
- 49 P. Akhter, F. Ali, A. Ali and M. Hussain, *Diamond Relat. Mater.*, 2024, **141**, 110702.
- 50 H. S. Shahraki, R. Bushra, N. Shakeel, A. Ahmad, Quratulen, M. Ahmad and C. Ritzoulis, *J. Bioresour. Bioprod.*, 2023, **8**, 162–175.
- 51 M. A. Ahmed, M. A. Ahmed and A. A. Mohamed, *Opt. Mater.*, 2024, **151**, 115339.
- 52 A. K. Chakraborty, S. Akter, S. Ganguli, M. A. Haque, A. S. M. Nur and M. A. Sabur, *Environ. Technol. Innovation*, 2024, **33**, 103536.
- 53 J. Yadav, S. Tripathi, S. P. Singh, P. Dwivedi, R. K. Rawat and P. Chauhan, *Chem. Inorg. Mater.*, 2025, **7**, 100113.
- 54 V. Elyasi, Y. Shaveisi and S. Sharifnia, *Mater. Chem. Phys.*, 2025, **329**, 130118.
- 55 Sonia, H. Kumari, Monica, S. Sharma, Reenu, R. Kumar, Suman, S. Chahal, S. Kumar, P. Kumar and A. Kumar, *J. Electron. Mater.*, 2024, **53**, 5990–6002.

